Phase Stability Effects on Hydrogen Embrittlement Resistance in Martensite Reverted Austenite Steels

Phase stability effects on hydrogen embrittlement resistance in martensite – reverted austenite steels

B. C. Cameron[1], M. Koyama[2] and C. C. Tasan[1,*]

[1]Department of Materials Science and Engineering, Massachusetts Institute of Technology, Cambridge, MA, 02139 USA

[2] Department of Mechanical Engineering, Kyushu University, Nishi-ku, Fukuoka 819-0395, Japan

*corresponding author: tasan@mit.edu

Abstract

Earlier studies have shown that interlath austenite in martensitic steels can enhance hydrogen embrittlement (HE) resistance. However, the improvements were limited due to micro-crack nucleation and growth. A novel microstructural design approach is investigated, based on enhancing austenite stability to reduce crack nucleation and growth. Our findings from mechanical tests, X-ray diffraction and scanning electron microscopy reveal that this strategy is successful. However, the improvements are limited due to intrinsic microstructural heterogeneity effects.

Keywords: *TRIP; EBSD; ECCI; damage; fracture*

Martensitic steels are high strength steels that are commonly used in the energy [1,2], automotive [3,4], and construction industries [5,6], however, their hydrogen embrittlement (HE) susceptibility limits their use [7,8]. One remedy for this is the introduction of a reverted nanoscale austenite phase (γ) which provides for substantial work hardening capacity through the transformation-induced plasticity (TRIP) mechanism [9–14]. For example, in a previous work a Fe-9Mn-3Ni-1.4Al-0.01C (mass %) martensitic steel was aged to introduce 36% of γ phase, which led to increases in ductility, both in H-free [15] and H-precharged states [16]. However, due to a "smaller is less stable" size effect, the majority of γ grains transform at relatively early stages of deformation, limiting the effectiveness of this approach [10]. It has been shown that these transformations also cause a significant local increase in the H chemical potential, increasing the crack nucleation probability in martensite (α') [14,17,18]. As a result, macroscopic failure begins with cracking along phase boundaries, following the early γ transformation[13].

Other TRIP steels also suffer from HE due to similar reasons: i.e., transformation of austenite, which has high solubility of hydrogen, to martensite, which is prone to HE, leads to early cracking [19,20]. This leads to an interesting conflict from the perspective of steel design. Although mechanically-induced martensitic transformation increases the strain hardening capacity of the material [21,22], it can also cause premature failure in the presence of H [23,24]. Thus, strategies that can enable the benefits of the TRIP effect, while not causing HE susceptibility, would be of interest for all industries and applications listed above. The microstructure design approach that is investigated here relies on introducing γ grains of a wider range of stability in order to spread the toughening effect of TRIP to a wider deformation range.

To implement this approach of altering the austenite stability, the same Fe-9Mn-3Ni-1.4Al-0.01C martensitic steel, referred to above, is subjected to altered thermomechanical processing

46 previously developed[11]. Specifically, a cold rolling step is introduced prior to annealing altering
47 the γ nucleation and growth kinetics. The sample is annealed for one hour to achieve a similar
48 phase fraction to previous HE investigations[16], however, the γ size distribution and
49 morphology is substantially altered with the γ grains becoming more equiaxed (Figures 1(a) and
50 (b)). It is this size distribution which leads to a wider range of γ stability[10], and improved
51 mechanical properties without H[11]. Here, samples subjected to this cold rolling and
52 thermomechanical processing are referred to as MA_{CR} and are compared to those with the
53 original processing MA. The sheet was cut, using electro discharge machining, into dog-bone
54 tensile samples with a gauge width of 2 mm and length of 4.9 mm. The surfaces were ground
55 with P800 grit grinding paper to remove a few microns of surface contamination, oxidation, any
56 damage from machining from previous processing steps, and to achieve a consistent surface
57 finish. The sample was cathodically charged with H in 5% H_2SO_4 aqueous solution and 3 g/L
58 NH_4SCN as a recombination poison, at a current density of 5 A/m^2 and using a counter
59 electrode of platinum foil. The charging time was computed using the diffusion scaling
60 relationship $t \sim l^2/D$ where t is the charging time, l is the length scale and $D = 3.7 \times 10^{-11}$ m^2/s is
61 the diffusion coefficient for martensitic steel [25]. A charging time of 14.4 ks was calculated using
62 the full thickness of the sample l to ensure that there was no H gradient toward the center of
63 the sample. The H charged samples are referred to as MA_{CR-H} and are compared to samples
64 charged in a similar manner in the previous study (MA_H) [16]. High resolution electron
65 backscatter detection (EBSD) measurements were carried out at 80 nm spatial resolution using
66 a Zeiss Merlin scanning electron microscope (SEM), equipped with an EDAX EBSD system,
67 running at 15 kV. Electron channeling contrast images (ECCI) images were obtained with a
68 probe current of 10 nA, a working distance of 6.4 mm and a voltage of 20 kV. Note that in the
69 ECCI analysis of these types of steels, martensite can be recognized due to maraging
70 precipitates and the austenite can be recognized due to the structure of the stacking faults [15].
71 This classification method (which is confirmed by EBSD) is used throughout this work in
72 identifying the present phases. Secondary electron (SE) images were used for damage
73 quantification and were obtained with a probe current of 2 nA, a working distance of 7.2 mm
74 and a voltage of 15 kV. X-ray diffraction (XRD) measurements were done employing a Bruker
75 general area diffraction detection system, using Cu Kα radiation (λ=1.54 Å) with a 0.1 mm spot
76 and a $0 - 90^o$ 2θ range. The phase fractions at different stages of deformation were computed
77 by comparing the γ (111) and (002) peak and the α' (011) peak using Rietveld analysis.
78
79
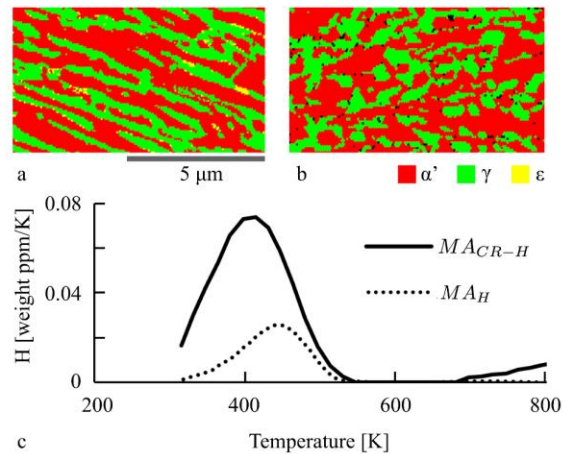
Fig. 1: EBSD phase maps of (a) MA, and (b) MA_{CR}[1]. Note the rolling direction is horizontal and the transverse direction is out of the page. (c) H desorption as a function of temperature for MA_{CR-H}, compared with MA_H [16]. Note that the MA_H heating rate and sample geometry were slightly different [16]. This may affect peak locations but should have little impact on the total H desorbed. The units ppm/K are used instead of the more conventional ppm/s to enable a direct comparison of the total H amount the two samples.

The H content and desorption rate were measured using thermal desorption analysis (TDA) (Figure 1(c)) [26]. For these experiments, a cuboidal sample (9 by 4 by 1 mm) was charged with H, inserted within 10 min into the vacuum chamber which reached vacuum in 88 min. The sample was then heated at a rate of 5.56×10^{-2} K/s. The H desorption of MA_{CR-H} as a function of temperature is compared to MA_H in Figure 1(c). The total H content of the MA_{CR-H} sample was 15.6 weight ppm which is significantly greater than the 1.87 ppm of MA_H sample. From the TDA data it is apparent that MA_{CR} has a substantially larger amount of hydrogen, which may be attributed to the higher density of trapping sites and/or the higher H diffusion rate into this microstructure [27].

Three MA_{CR} samples and three MA_{CR-H} samples were mechanically tested in uniaxial tension using an Instron 4201 machine. The stress strain response is compared with MA and MA_H in Figure 2(a). A cross head displacement was chosen to correspond to a gauge strain rate of 10^{-3} s^{-1}. Strain measurements were carried out using digital image correlation (DIC) and processed using Ncorr software [28]. The XRD phase fractions and the damage statistics were measured at different points along the sample where the strain is known from DIC (Figures 2(b) through (d)). Note that for two samples the time between charging and mechanical testing was minimized to limit H desorption out of the sample (24 and 21 min) whereas the third sample the time, normalized by l^2/D, was set to equal to MA_H[16] so the results could be compared (135 min). Nevertheless, both configurations produced the same mechanical properties which is unsurprising as there is little H desorption at room temperature (Figure 1(c)).

---

[1] Note that an ε-martensite phase that occurs is an intermediate phase that can occur during the $\gamma \rightarrow \alpha'$ transformation, though it is relatively stable during deformation[10,35,36].

109
110
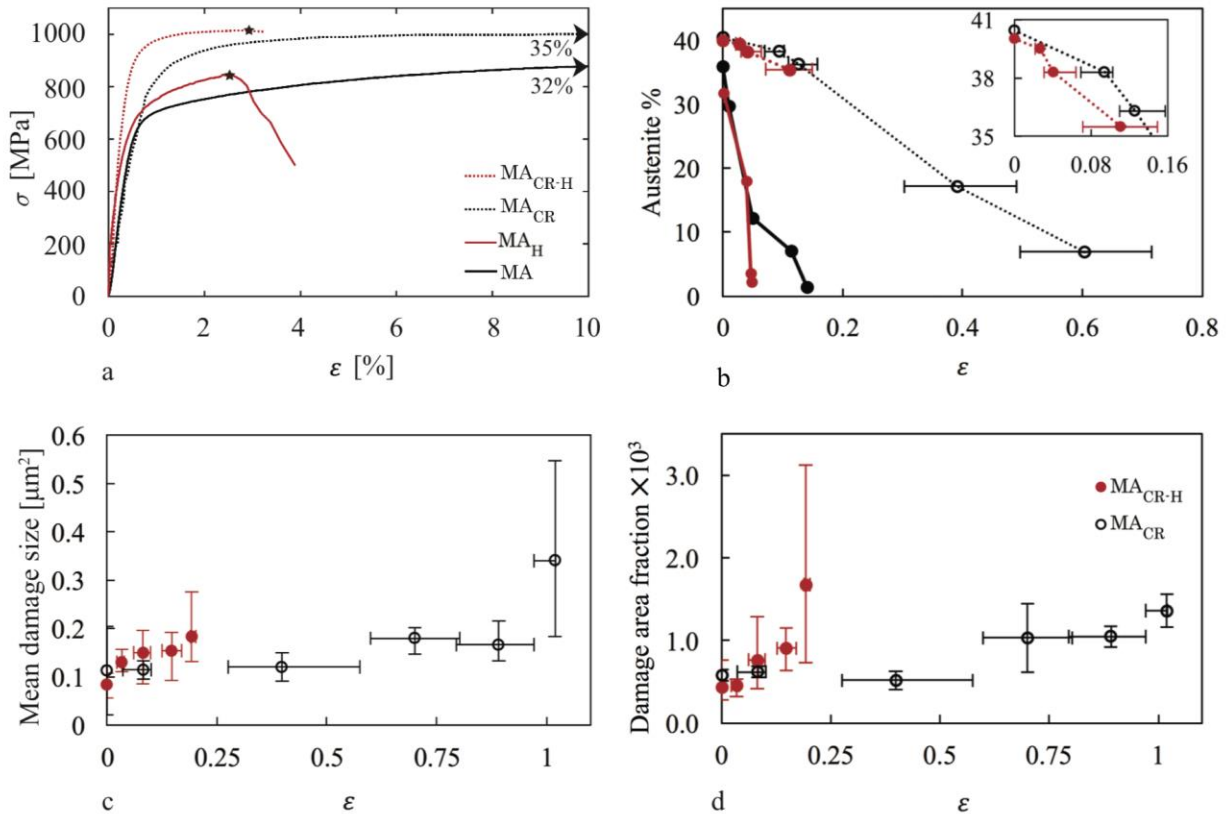
111
112 *Fig. 2: (a) Engineering stress vs. strain plots of the discussed steels with and without H charging. Stars indicate the*
113 *uniform elongation. (b) Austenite stability as a function of the local ε_{yy} strain (y is the loading direction) in*
114 *MA_{CR-H} and MA_{CR}, in comparison to that of MA [15]. The inset shows a zoomed-in comparison. (c-d) The mean*
115 *damage size and the damage area fraction as a function of the local ε_{yy} strain in MA_{CR-H} and MA_{CR}. The*
116 *horizontal error bars reflect the range of strain values over which the phase and damage statistics were obtained.*
117 *The vertical error bars reflect the range of values obtained by computing the damage statistics over different*
118 *microstructural regions subjected to the same strain.*

119
120 The results of these experiments show an improvement of the strength – ductility combination
121 in MA_{CR-H} compared to MA_H (Figure 2(a)). The ultimate tensile strength increases from 829 to
122 1014 MPa, however the uniform elongation remains similar (it slightly increases from 2.8% to
123 3.1%[2]). Note that, given its higher strength and H content (Figure 1(c)), MA_{CR} would have been
124 expected to be more susceptible to HE. The XRD results show that the γ phase has increased
125 mechanical stability in MA_{CR-H} when compared to MA_H (Figure 2(b)), as intended by the
126 design strategy to reduce the TRIP induced damage nucleation. The success of this
127 microstructural design strategy is further demonstrated by two microscopic observations. First,
128 examination over large, highly deformed, regions using SE imaging and ECCI (for example
129 Figures 3(a) and (b)) reveals substantially reduced crack nucleation incidents in the vicinity of

---

[2] Comparison is made using the mean of the three MA_H samples and the single MA_{CR-H} sample with an
equivalent time between H charging and mechanical testing, though the other MA_{CR-H} samples had similar
mechanical properties.

130 transformed γ grains for MA_{CR-H} (of the kind shown in Figure 3(c)), compared to MA_H [16] 3.
131 These voids are only observed in the highly deformed regions of the sample, indicating that
132 they are deformation induced. Absence of a large crack density in the vicinity of these grains
133 reduces probability of crack coalescence leading to early macroscopic failures as in MA_H.
134 Second, the increased γ volume fraction at higher strains enables the microstructure to
135 effectively arrest those cracks that are nucleated (Figure 3(d)). In fact, there is not an increase
136 in mean damage size in MA_{CR-H} compared to MA_{CR} (Figure 2(c)), despite H pre-charging. In
137 summary, following the implementation of the microstructural design strategy, the nucleation
138 and coalescence failure mechanism, observed in MA_H, is no longer observed.

139
140
141
142
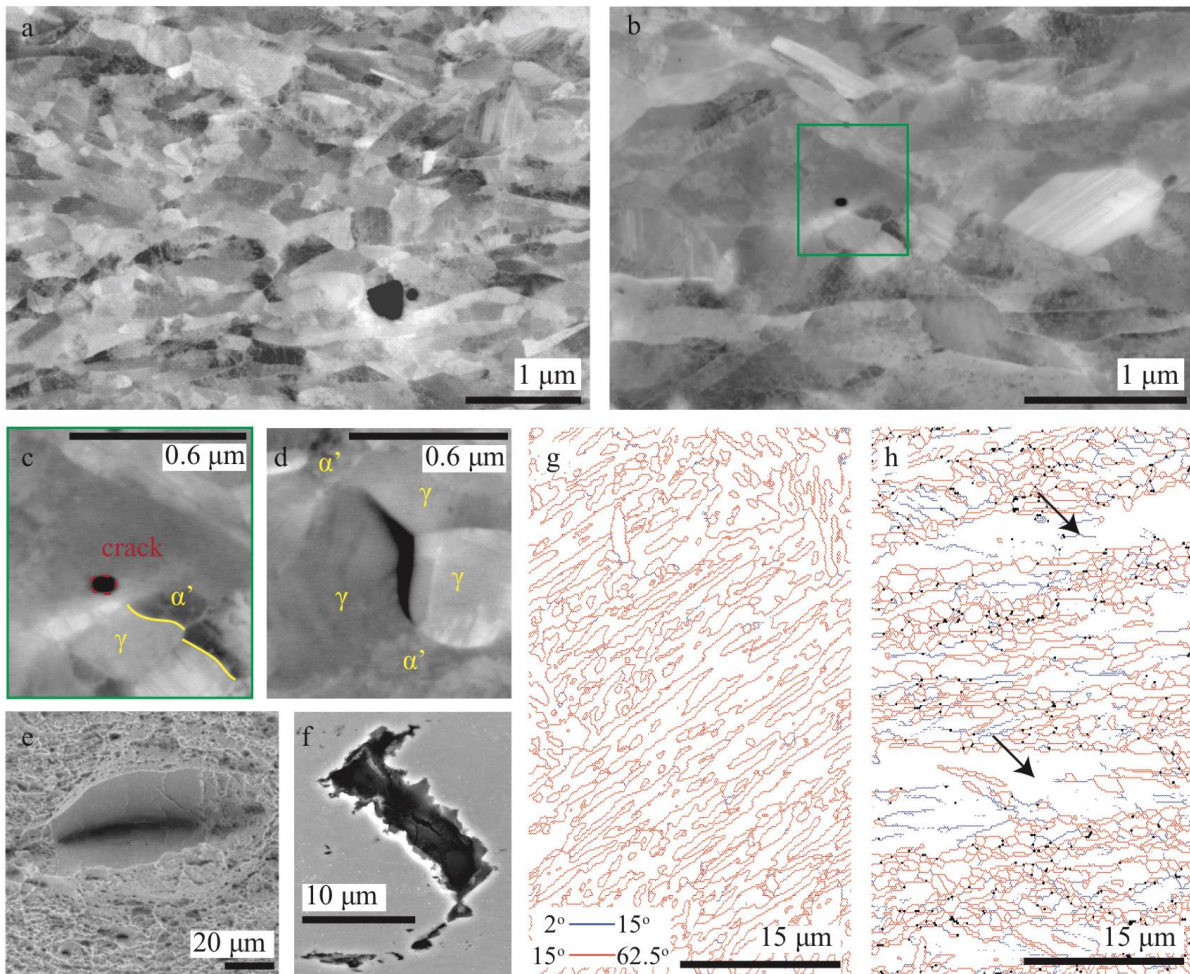
143

---

144 *Fig. 3: (a-d) ECC images of the highly deformed neck region of a MA_{CR-H} sample. (c) A crack nucleation in the*
145 *vicinity of a transforming γ grain. (d) A crack arrested without growing significantly bigger than the average grain*
146 *size. (e) Fracture surface of the MA_{CR-H} by SE imaging. (f) SE image of a large damage event in the highly*
147 *deformed neck region of MA_{CR-H}. (g-h) EBSD obtained grain boundaries in MA (left) and MA_{CR} (right)* [11]. *Note the*
148 *rolling direction is horizontal and the transverse direction is out of the page.*
149

150 Given these points, specifically the higher γ volume fraction and strain hardening capacity at
151 higher deformation levels [9], it is not immediately clear why even a higher improvement in HE
152 resistance is not achieved in MA_{CR-H}. The remainder of this report is focused on elucidating
153 the failure mechanism that is activated in this material, to provide insight into further
154 microstructural design strategies that may be employed in future.
155

156 As can be seen in Figure 2(d), there is a surprisingly large variance in the damage area fraction
157 just before failure, indicating a heterogeneous damage distribution. SE examination reveals that
158 this is attributed to a few large damage events with length scales of 10-100 μm, significantly
159 larger than the average grain size of less than 1 μm (Figure 3(f)). Note that this is not reflected
160 significantly in the mean damage size (Figure 2(c)) as these large damage events are only a
161 small number fraction of the total damage events. These large damage events were also
162 observed on the fracture surface and, unlike other areas of the fracture surface, did not exhibit
163 ductile features, such as dimples, suggesting they occurred primarily in martensite and are
164 characteristic of HE (Figure 3(e))[29,30]. EBSD analysis reveals that in MA_{CR} there are indeed large
165 regions of high martensite content with a low density of internal high angle boundaries unlike
166 MA (Figures 3(g) and (h), see arrows). It is in these locations that the large damage events occur.
167 This microstructural heterogeneity is introduced due to the cold rolling process, where the
168 grain subdivision occurs at different deformation levels that depend on their respective
169 crystallographic orientations [31]. If the deformation level during cold rolling is not sufficiently
170 high, as in this case, a fraction of the grains will not undergo subdivision [32]. The resulting
171 absence of high angle grain boundaries in the prior austenitic grains will reduce the number of
172 γ nucleation events during annealing [11], resulting in the large martensitic regions observed.
173 Furthermore, a number of inclusions cause cracking in the steel during the cold rolling process
174 (Figure 4(a)). These cracks, existing prior to final deformation, can be large relative to the
175 average grain size, and are often observed at the boundaries of these large martensitic regions.
176
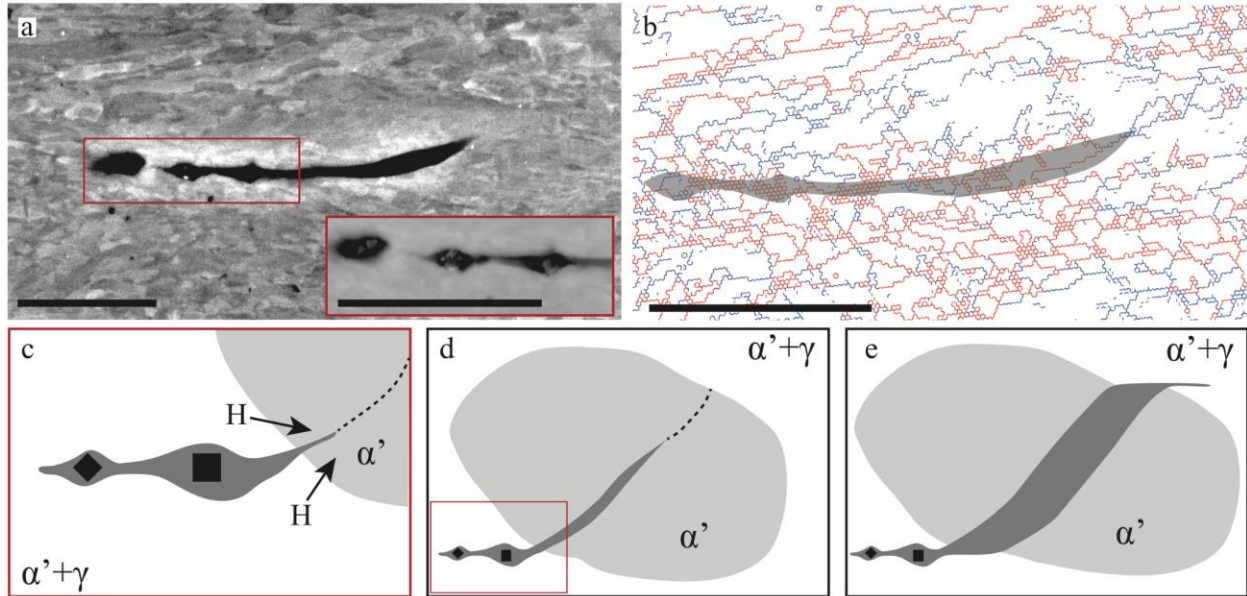
Fig. 4: (a) Backscatter electron imaging of crack nucleation at inclusions, and crack propagation through a martensitic region. (b) EBSD grain boundary image of the same region. Note the rolling direction is horizontal and the transverse direction is out of the page. (c-e) schematic description of the proposed failure mechanism. Scale bars are 4 μm.

The combination of large voids caused by inclusions, excess hydrogen activity due to $\gamma \rightarrow \alpha'$ transformation[33], and large martensitic regions that are susceptible to HE, give the necessary conditions for significant crack growth (Figures 4(a) and (b)). This crack growth occurs despite a significant γ fraction in other areas of the material due to its heterogeneous distribution. These growing cracks are eventually arrested when they reach the boundaries of the martensitic regions, resulting in the large damage events frequently observed. Due to their size, these damage events will have significant stress concentrations at their crack tips [34]. As the deformation proceeds, both the number of these large damage events will increase, increasing the average stress in the surrounding material, and the γ fraction will decrease, decreasing the materials crack arresting ability. Eventually, these factors will overcome the crack arresting ability of the γ, leading to final fracture throughout the α' and γ region, that propagates primarily through a crack nucleation, growth and coalescence mechanism. This sequence of events, illustrated in Figures 4(c) through (e), explains the surprising observation of a significant γ fraction at failure (Figure 2(b)).

In summary, the influence of phase stability and interface characteristics on HE resistance in TRIP steels was investigated. This strategy resulted in both increased strength and uniform elongation, overcoming the strength ductility tradeoff in high strength steels subjected to H. In addition, the failure mechanism of successive nucleation and coalescence of multiple cracks, that exist in alternate alloys, is not observed. However, the large α' allow unconstrained cleavage type growth leading to failure; mitigating the improvements made to the uniform elongation. This insight indicates that eliminating the primarily α' regions will lead to further

increases in ductility while retaining the increased strength. This may be achieved, for martensite- reverted austenite steels, by finding ways to homogenize the microstructure while retaining these favorable γ transformation properties, possibly by increasing the cold rolling level.

References

1   G. Yagawa, Y. Kanto, S. Yoshimura, H. Machida, and K. Shibata: *Nucl. Eng. Des.*, 2001, vol. 207, pp. 269–86.

2   J. Pierre, R. Francois, and P. Christophe: in *Proceedings of the ASME 2013 Pressure Vessels and Piping Conference*, Paris, 2013, pp. 1–8.

3   G. Lovicu, M. Bottazzi, F.D. Aiuto, M.D.E. Sanctis, A. Dimatteo, and C. Santus: *Meallurgical Mater. Trans. A*, 2012, vol. 43, pp. 4075–87.

4   M. Loidl, O. Kolk, S. Veith, and T. Göbel: *Materwiss. Werksttech.*, 2011, vol. 42, pp. 1105–10.

5   J. Capelle, J. Gilgert, I. Dmytrakh, and G. Pluvinage: *Int. J. Hydrogen Energy*, 2008, vol. 33, pp. 7630–41.

6   M. Perrin, L. Gaillet, C. Tessier, and H. Idrissi: *Corros. Sci.*, 2010, vol. 52, pp. 1915–26.

7   M. Koyama, E. Akiyama, K. Tsuzaki, and D. Raabe: *Acta Mater.*, 2013, vol. 61, pp. 4607–18.

8   M. Koyama, C.C. Tasan, E. Akiyama, K. Tsuzaki, and D. Raabe: *Acta Mater.*, 2014, vol. 70, pp. 174–87.

9   R. a. McCoy and W.W. Gerberich: *Metall. Trans.*, 1973, vol. 4, pp. 539–47.

10   M.M. Wang, C.C. Tasan, D. Ponge, A. Kostka, and D. Raabe: *Acta Mater.*, 2014, vol. 79, pp. 268–81.

11   M.M. Wang, C.C. Tasan, D. Ponge, and D. Raabe: *Acta Mater.*, 2016, vol. 111, pp. 262–72.

12   M. Koyama, Z. Zhang, M. Wang, D. Ponge, D. Raabe, K. Tsuzaki, H. Noguchi, and C.C. Tasan: *Science.*, 2017, vol. 355, pp. 1055–7.

13   R. a. McCoy, W.W. Gerberich, and V.F. Zackay: *Metall. Trans.*, 1970, vol. 1, pp. 2031–4.

14   Y.D. Park, I.S. Maroef, A. Landau, and D.L. Olson: *Weld. Res.*, 2002, pp. 27–35.

15   M.M. Wang, C.C. Tasan, D. Ponge, A.C. Dippel, and D. Raabe: *Acta Mater.*, 2015, vol. 85, pp. 216–28.

16   M. Wang, C.C. Tasan, M. Koyama, D. Ponge, and D. Raabe: *Metall. Mater. Trans. A*, 2015, vol. 46, pp. 0–5.

17   J.Y. Lee and S.M. Lee: *Surf. Coatings Technol.*, 1986, vol. 28, pp. 301–14.

18   K.G. Solheim, J.K. Solberg, J. Walmsley, F. Rosenqvist, and T.H. Bjørnå: *Eng. Fail. Anal.*, 2013, vol. 34, pp. 140–9.

19   J.H. Ryu, Y.S. Chun, C.S. Lee, H.K.D.H. Bhadeshia, and D.W. Suh: *Acta Mater.*, 2012, vol.

249   60, pp. 4085–92.

250   20   J. Han, J.H. Nam, and Y.K. Lee: *Acta Mater.*, 2016, vol. 113, pp. 1–10.

251   21   G. Frommeyer, U. Brüx, and P. Neumann: *ISIJ Int.*, 2003, vol. 43, pp. 438–46.

252   22   E. De Moor, S. Lacroix, A.J. Clarke, J. Penning, and J.G. Speer: *Metall. Mater. Trans. A*,
253   2008, vol. 39, p. 2586.

254   23   T. Michler, C. San Marchi, J. Naumann, S. Weber, and M. Martin: *Int. J. Hydrogen Energy*,
255   2012, vol. 37, pp. 16231–46.

256   24   J. Sojka, V. Vodárek, I. Schindler, C. Ly, M. Jérôme, P. Váňová, N. Ruscassier, and A.
257   Wenglorzová: *Corros. Sci.*, 2011, vol. 53, pp. 2575–81.

258   25   W.C. Luu and J.K. Wu: *Corros. Sci.*, 1996, vol. 38, pp. 239–45.

259   26   P.A. Redhead: *Vacuum*, 1962, vol. 12, pp. 203–11.

260   27   M. Nagumo: *Fundamentals of Hydrogen Embrittlement*, Springer, Singapore, 2016.

261   28   J. Blaber, B. Adair, and A. Antoniou: *Exp. Mech.*, 2015, vol. 55, pp. 1105–22.

262   29   A. Nagao, C.D. Smith, M. Dadfarnia, P. Sofronis, and I.M. Robertson: *Acta Mater.*, 2012,
263   vol. 60, pp. 5182–9.

264   30   M.L. Martin, B.P. Somerday, R.O. Ritchie, P. Sofronis, and I.M. Robertson: *Acta Mater.*,
265   2012, vol. 60, pp. 2739–45.

266   31   J.L. Zhang, C.C. Tasan, M.L. Lai, J. Zhang, and D. Raabe: *J. Mater. Sci.*, 2015, vol. 50, pp.
267   5694–708.

268   32   R. Ueji, N. Tsuji, Y. Minamino, and Y. Koizumi: *Sci. Technol. Adv. Mater.*, 2004, vol. 5, pp.
269   153–62.

270   33   X. Zhu, W. Li, H. Zhao, L. Wang, and X. Jin: *Int. J. Hydrogen Energy*, 2014, vol. 39, pp.
271   13031–40.

272   34   A.A. Griffith: *Philos. Trans. R. Soc. london. Ser. A*, 1921, vol. 221, pp. 163–98.

273   35   Y.S. Chun, J.S. Kim, K.T. Park, Y.K. Lee, and C.S. Lee: *Mater. Sci. Eng. A*, 2012, vol. 533, pp.
274   87–95.

275   36   T.H. Lee, E. Shin, C.S. Oh, H.Y. Ha, and S.J. Kim: *Acta Mater.*, 2010, vol. 58, pp. 3173–86.

276

277

278 *Fig. 1: EBSD phase maps of (a) MA, and (b) MA_{CR}[4]. Note the rolling direction is horizontal and the transverse*
279 *direction is out of the page. (c) H desorption as a function of temperature for MA_{CR-H}, compared with MA_H [16].*
280 *Note that the MA_H heating rate and sample geometry were slightly different [16]. This may affect peak locations but*
281 *should have little impact on the total H desorbed. The units ppm/K are used instead of the more conventional*
282 *ppm/s to enable a direct comparison of the total H amount the two samples.*
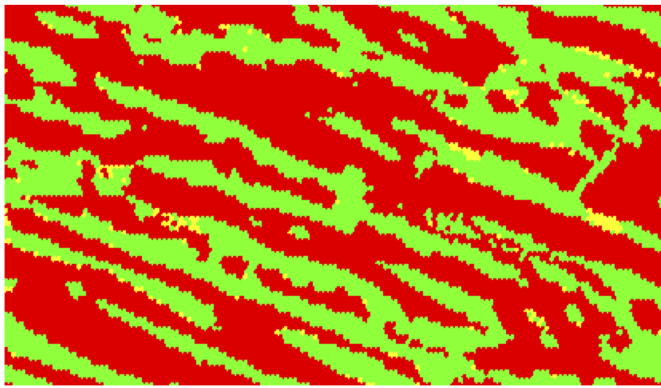
283

284 *Fig. 2: (a) Engineering stress vs. strain plots of the discussed steels with and without H charging. Stars indicate the*
285 *uniform elongation. (b) Austenite stability as a function of the local ε_{yy} strain (y is the loading direction) in*
286 *MA_{CR-H} and MA_{CR}, in comparison to that of MA [15]. The inset shows a zoomed-in comparison. (c-d) The mean*
287 *damage size and the damage area fraction as a function of the local ε_{yy} strain in MA_{CR-H} and MA_{CR}. The*
288 *horizontal error bars reflect the range of strain values over which the phase and damage statistics were obtained.*
289 *The vertical error bars reflect the range of values obtained by computing the damage statistics over different*
290 *microstructural regions subjected to the same strain.*

291

---

4 *Note that an ε-martensite phase that occurs is an intermediate phase that can occur during the $\gamma \rightarrow \alpha'$*
transformation, though it is relatively stable during deformation[10,35,36].

292 *Fig. 3: (a-d) ECC images of the highly deformed neck region of a MA_{CR-H} sample. (c) A crack nucleation in the*
293 *vicinity of a transforming γ grain. (d) A crack arrested without growing significantly bigger than the average grain*
294 *size. (e) Fracture surface of the MA_{CR-H} by SE imaging. (f) SE image of a large damage event in the highly*
295 *deformed neck region of MA_{CR-H}. (g-h) EBSD obtained grain boundaries in MA (left) and MA_{CR} (right) [11]. Note the*
296 *rolling direction is horizontal and the transverse direction is out of the page.*
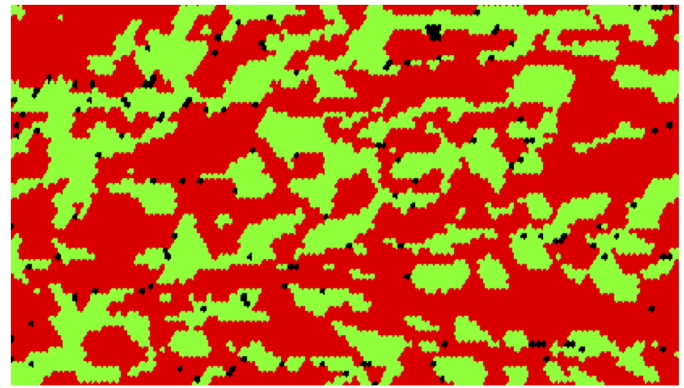297
298 *Fig. 4: (a) Backscatter electron imaging of crack nucleation at inclusions, and crack propagation through a*
299 *martensitic region. (b) EBSD grain boundary image of the same region. Note the rolling direction is horizontal and*
300 *the transverse direction is out of the page. (c-e) schematic description of the proposed failure mechanism. Scale*
301 *bars are 4 μm.*
302

a

b

α'   γ   ε

5 μm

MA_{CR-H}

MA_H

c

a

b

c

d

a

crack

α'

γ

0.6 μm

b

α'

γ

γ

γ

α'

0.6 μm

c

20 μm

d

10 μm

e

2° ——— 15°

15° ——— 62.5°

15 μm

f

15 μm